PCCP

ROYAL SOCIETY OF CHEMISTRY

PAPER

View Article Online
View Journal | View Issue

Cite this: *Phys. Chem. Chem. Phys.*, 2026, **28**, 7051

Revealing the N_2 gas-induced gate-opening in Mn-ZIF-8 and Cu-ZIF-8 from the perspective of *in situ* EPR spectroscopy

Antareekshya Deka, [a] Muhammad Fernadi Lukman, [a] Sibo Chetry, [b] Christian Jänke, [b] Harald Krautscheid [b] and Andreas Pöppl *[a]

Received 8th December 2025,
Accepted 11th February 2026

DOI: 10.1039/d5cp04761g

rsc.li/pccp

The structural transition of ZIF-8 under N_2 gas adsorption/desorption processes has been already investigated using various characterization techniques. This study demonstrates that electron paramagnetic resonance (EPR) spectroscopy is an alternative and powerful method that provides valuable local structure insights into the gate opening from ambient pressure (AP) to high pressure (HP) structural phases of the ZIF-8 framework during N_2 gas adsorption/desorption. Our *in situ* EPR experiments reveal distinct distortions in the environment of the tetrahedral metal ion framework sites for Mn^{2+} and Cu^{2+} dopants, demonstrating their different responsiveness to the gate opening transition. We were able to detect the AP to HP structural transition by monitoring the changes in the zero-field splitting of the paramagnetic Mn^{2+} (S = 5/2) probe ions. The results are complemented by employing Cu^{2+} (S = 1/2) centres as alternative spin probes where the Cu^{2+} g-tensor and hyperfine parameters change likewise at the AP to HP structural transition. Our findings validate the use of paramagnetic centres as spin probes for locally monitoring the N_2 gas-induced structural changes within the ZIF-8 framework. Notably, *in situ* EPR spectroscopy was successfully utilised to observe such transitions during N_2 gas adsorption/desorption processes in ZIF-8. The acquired spectroscopic results are consistent with previous reports on the gate-opening of ZIF-8, confirming the reliability and potential of this local spectroscopic method.

Introduction

Metal–organic frameworks (MOFs) have captured attention as some of the most explored porous materials.[1–4] They are widely known for their exceptional properties like high porosity, large surface area, framework flexibility, *etc.*, which make them utilizable for numerous potential applications such as gas adsorption, separation, drug delivery and storage, catalysis, and so on.[1–3] The crystalline network of MOFs is formed by coordination bonds between metal ions and organic linkers and exhibits structural variability and, in some cases, flexibility, which allows the framework to have structural transformations such as the ''breathing'' or ''gate-opening'' effect.[5–7] The flexibility of such materials, where the framework expands or contracts, can be induced by external stimuli such as the adsorption of guest molecules, temperature, or pressure variations.[5]

Among many intensively studied MOFs, zeolitic imidazolate framework-8 (ZIF-8) stands out because of its exceptional thermal and chemical stability as compared to other MOFs.[8] ZIF-8 has a sodalite (**sod**) topology and is formed by tetrahedral units, containing one Zn^{2+} cation and four methyl-imidazolate anions (Fig. 1a).[9,10] The imidazolate linkers generate large cages with a diameter of 11.6 Å interconnected through narrow windows with a diameter of 3.4 Å.[9] Despite having a relatively robust framework, ZIF-8 still manages to exhibit a unique ''swing-effect'' phenomenon[7,10–13] upon being exposed to certain guest molecules such as N_2, CH_4 and CO_2,[14] as well as framework deformation upon the adsorption of CO, O_2 and Ar.[15] Recent experimental and theoretical studies have shown that ZIF-8 undergoes gas-induced rotation of the methyl imidazolate linkers, where the $-CH_3$ groups rotate outwards and thereby clearing the four-membered narrow window (Fig. 1b), which is responsible for the ''gate-opening'' effect in response to the adsorption process of certain gases.[10,13–17] Previous work analysed the structural changes from ambient pressure (AP) to high-pressure (HP) phases of ZIF-8, using hydrostatic pressure and high-pressure diffraction experiments.[18] Therefore, in this work, the terms AP and HP are used to describe this

[a] *Felix Bloch Institute for Solid State Physics, Leipzig University, 04103 Leipzig, Germany. E-mail: poeppl@physik.uni-leipzig.de*
[b] *Institute of Inorganic Chemistry and Crystallography, Leipzig University, 04103 Leipzig, Germany*

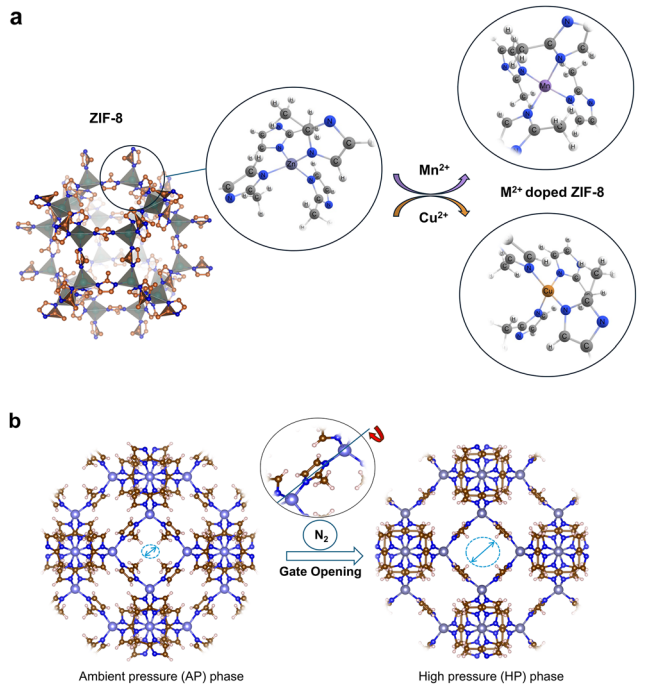

Fig. 1 (a) Structural representation of ZIF-8 and the Zn^{2+} tetrahedral sites, which are replaced by approximately 0.017% of Mn^{2+} and 0.41% of Cu^{2+} ions, respectively. (b) Schematic of the ZIF-8 gate opening from the ambient pressure (AP) phase to the high pressure (HP) phase induced by the adsorption of N_2 gas. The inset shows the Me-Im group together with its rotational axis at the advent of N_2 gas-induced gate opening.

gate-opening phenomenon, induced by the aforementioned swinging effect.

Various experimental techniques, like inelastic neutron scattering,[7] X-ray absorption spectroscopy,[19] powder XRD measurements[6] and Raman spectroscopy[13] have already been used to provide detailed insights into the adsorption behaviour of ZIF-8. All these methods consistently suggest that gas-induced structural deformation in the ZIF-8 framework arises solely due to the swinging of the imidazolate linker, with no further significant structural deformation of the framework upon gas exposure. While these methods successfully demonstrated the rotation of the methyl imidazolate linkers, where the methyl groups facilitate access to the voids upon N_2 adsorption, there is still a lack of details regarding the effect of the gate-opening mechanism towards the Zn^{2+} local structure. From the perspective of the Zn^{2+} local structure, solid-state ^{67}Zn NMR spectroscopy has been implemented to verify the almost perfect tetrahedral coordination of Zn^{2+} in the ZIF-8 framework.[20] So far, there is no experimental evidence that this tetrahedral zinc site is affected by the gate opening.[20] In contrast, it has been predicted that replacing Zn^{2+} with other bivalent metal ions such as Fe^{2+} or Mg^{2+} has a significant influence on the ZIF-8 gate-opening energy.[21]

On the other hand, electron paramagnetic resonance (EPR) spectroscopy is a very powerful complementary technique that directly monitors how the gas molecules interact with the paramagnetic centres incorporated into the framework and also detects structural changes of the framework in the close proximity of the paramagnetic ions induced by sorption of guest molecules.[22–26] In the present study, we have employed *in situ* continuous wave (CW) EPR measurements to investigate the gate-opening transformation of the ZIF-8 framework upon N_2 gas sorption processes. In this work, paramagnetic centres like Mn^{2+} and Cu^{2+} ions were doped into the ZIF-8 framework *via* substitution of Zn^{2+} metal sites, making those substituted metal sites accessible for monitoring the N_2 gas-induced gate-opening transformation and local structural changes in their environment by *in situ* continuous wave (CW) EPR spectroscopy.

In a previous study,[27] the successful incorporation of Cu^{2+} into the Zn^{2+} lattice sites of the ZIF-8 framework has already been verified using CW and pulsed EPR spectroscopy at low temperatures ($T \leq 20$ K) supported by quantum chemical computation based on density functional theory (DFT).[27] Separately, the ZIF-8 system fully based on Mn^{2+} has been realised by Kadota and co-workers.[28] Therefore, it seems justified to assume that Mn^{2+} can also be doped into the ZIF-8 framework, expecting a substitution at the Zn^{2+} metal sites. In order to validate the incorporation of Mn^{2+} ions on the tetrahedral zinc framework sites, X- and Q-band CW EPR experiments were carried out on the Mn^{2+} doped ZIF-8 material (Mn-ZIF-8). As the AP to HP structural transformation during N_2 adsorption occurs in the temperature range of 60 K $\leq T \leq$ 80 K,[6,7] the temperature dependencies of both Mn^{2+} and Cu^{2+} EPR signals were also investigated in order to examine structural peculiarities in comparison to the parent Zn^{2+} sites. On the basis of this preliminary work, *in situ* CW EPR experiments during N_2 gas adsorption and desorption for both paramagnetic probe ions were performed to investigate the AP to HP structural transformation. The experiments revealed distinct changes in the spin Hamiltonian parameters of the paramagnetic probe ions (Mn^{2+} and Cu^{2+}) during N_2 gas sorption, suggesting that the AP $\leftrightarrow$ HP transformation and the related swinging effect of the methyl imidazolate linkers are accompanied by structural, albeit minor, distortions at the Mn^{2+} and Cu^{2+} tetrahedra.

Experimental section

Sample preparation

Materials. The following chemicals were used as received without further purification: zinc nitrate hexahydrate (98%, Aldrich), manganese chloride tetrahydrate (98%, Aldrich), copper nitrate trihydrate (99.5%, Merck), 2-methylimidazole (Hmim, 99%, TCI), and methanol ($\geq$99.9%, VWR).

Synthesis of Mn^{2+}-doped ZIF-8

Mn-ZIF-8 samples were synthesized following the method reported by Schejn *et al.*[29] Two separate methanolic solutions were prepared: one containing a total of 1 mmol of $Zn(NO_3)_2 \cdot 6H_2O$ and 0.01 mmol $MnCl_2 \cdot 4H_2O$ in 11.3 mL of methanol, and another containing 8 mmol Hmim dissolved in an equal volume of methanol. The Hmim solution was added dropwise to the metal chloride solution while stirring continuously at

room temperature. After 1 hour of stirring, the resulting Mn-ZIF-8 crystals were collected *via* centrifugation at 4000 rpm for 15 minutes, washed three times with 30 mL of methanol, and dried under ambient conditions overnight. The dried samples were thermally activated by heating at 200 °C for 6 hours in a programmable oven, followed by natural cooling to room temperature. To remove guest solvents, the samples were subjected to Soxhlet extraction with methanol, followed by evacuation at ambient temperature prior to the measurements. The activated samples were stored in Schlenk flasks at room temperature until further use.

Synthesis of Cu-doped ZIF-8

Cu-ZIF-8 was synthesized using the same procedure as that described for Mn-ZIF-8, with the $MnCl_2{\cdot}4H_2O$ replaced by $Cu(NO_3)_2{\cdot}3H_2O$ in equivalent molar proportions. All other steps remained unchanged.

Characterization

Quantitative analysis of zinc, manganese and copper content in the prepared Mn-ZIF-8 and Cu-ZIF-8 samples was performed using an inductively coupled plasma optical emission spectrometer (ICP-OES), specifically the PerkinElmer Optima 8000 model. Powder X-ray diffraction (PXRD) measurements were carried out using a STOE STADI-P diffractometer, operating with Cu-$K_{\alpha1}$ radiation (λ = 1.54060 Å). The activated samples were filled into glass capillaries (Hilgenberg) with an outer diameter of 0.5 mm and measured at room temperature. Thermogravimetric analysis (TGA) was done using a STA 449 F1 Jupiter thermobalance (Netzsch), with samples placed in corundum crucibles. For analysis of the volatile thermolysis products, the thermobalance was coupled to an Aeolos QMS 403C quadrupole mass spectrometer. Heating was performed at a constant rate of 10 K min^{-1} up to 900 °C under a continuous flow of high-purity argon (99.999%). N_2 adsorption studies at 77 K were conducted using a Belsorp-max G instrument (Microtrac, Version 1.1.0). For accurate dead volume assessment, helium gas of 99.998% purity was utilized, and N_2 of the same grade was used for the adsorption experiments. The scanning electron microscopy (SEM) images of the samples were acquired with a LEO Gemini 1530 SEM from Zeiss with an accelerating voltage of 20 kV.

EPR measurements

CW X-band (~9.4 GHz) measurements were done on both Mn-ZIF-8 and Cu-ZIF-8 using a Bruker EMX micro-spectrometer, equipped with a He Cryostat ESR900 from Oxford Instruments. For the temperature-dependent measurements on both samples, the microwave power was set to 0.06 mW, and the modulation amplitude and frequency were set to 5 G and 100 kHz, respectively. CW Q-band (~34 GHz) measurements were also carried out on Mn-ZIF-8 using a Bruker EMX 10–40 spectrometer, equipped with a He Cryostat CF935 from Oxford Instruments. The microwave power was adjusted to 0.06 mW, while the modulation amplitude and frequency were kept at 5 G and 100 kHz, respectively.

In situ CW X-band EPR measurements were performed while exposing both Mn-ZIF-8 and Cu-ZIF-8 to N_2 gas adsorption–desorption processes with varying pressures. A home-built gas loading station was used for dosing N_2, which facilitates *in situ* EPR experiments with different gases at absolute gas pressures from p = 0.001 mbar all the way up to p = 1330 mbar.[22] In the present study, we used N_2 gas from Linde (purity of 99.999%). For the *in situ* EPR measurements of Mn-ZIF-8, the temperature was set to 66 K, where the N_2 saturated vapour pressure was p^0 = 221 mbar. Moreover, the microwave power at the X-band spectrometer was adjusted to 0.6 mW, while the modulation amplitude and frequency modulation were kept at 5 G and 100 kHz, respectively.

For supplementary *ex situ* CW EPR measurements, the parent Mn-ZIF-8 MOF was transferred into conventional X- and Q-band quartz glass EPR tubes and activated at 150 °C for 12 hours on a vacuum line. Subsequently the samples were loaded with N_2 gas (400 mbar for X-band and 750 mbar for Q-band samples) and sealed.

All the EPR spectra were simulated with the help of the MATLAB simulation package EasySpin.[30] In the case of Mn^{2+} with total electron spin S = 5/2 simulations were done on the basis of the following spin Hamiltonian operator:[31]

$$\hat{H} = \mu_B \vec{\boldsymbol{B}}\boldsymbol{g}\hat{\vec{S}} + \hat{\vec{S}}\boldsymbol{A}\hat{\vec{I}} + \sum_k \sum_q B_k^q \hat{O}_k^q\left(\hat{\vec{S}}\right) \quad (1)$$

where the first term is the electron Zeeman interaction term, μ_B is Bohr's magneton, $\hat{\vec{S}}$ is the electron spin operator, and $\boldsymbol{g}$ is the g-tensor of the Mn^{2+} ion in the applied external magnetic field $\vec{\boldsymbol{B}}$. The second term describes the hyperfine (hf) interaction between the electron spin and the nuclear spin I = 5/2 of the ^{55}Mn isotope. The quantity $\boldsymbol{A}$ is the hf coupling tensor and $\hat{\vec{I}}$ the nuclear spin operator. Isotropic tensors $\boldsymbol{g}$ and $\boldsymbol{A}$ were used for the simulation of the Mn^{2+} spectra. The last term describes the zero-field splitting (ZFS), expressed in terms of a linear combination of extended Stevens operators $\hat{O}_k^q$.[32,33] Here, k = 2, 4 and $q = k, k-1, \ldots, -k$. B_k^q gives the magnitude of the corresponding zero-field splitting and $\hat{O}_k^q$ represents various operators of the total electron spin.[34] The parameters $D = 3B_2^0$ and $E = B_2^2$ correspond to the axial and orthorhombic second-order ZFS parameters, respectively, and were included in all spectral simulations. The impact of the higher-order ZFS parameters B_4^0, B_4^2, B_4^3 and B_4^4 (ref. 31 and 35) on the computed Mn^{2+} spectra was tested and where necessary also included in the simulation approach.

In the case of Cu^{2+}, spectral simulations were implemented according to the first and second terms of the spin Hamiltonian in eqn (1) where anisotropic tensors $\boldsymbol{g}$ and $\boldsymbol{A}$ have been employed. Here for Cu^{2+}, the second term indicates the hf interaction of the electron spin (S = 1/2) with the I = 3/2 nuclear spin of the copper isotopes ^{63}Cu and ^{65}Cu.

Results

Mn-ZIF-8

PXRD and ICP-OES were employed to confirm the structural integrity of the ZIF-8 framework and the presence of manganese in the Mn-ZIF-8 sample. The PXRD pattern (SI, Fig. S1a) of as synthesized Mn-ZIF-8 exactly matches the simulated pattern derived from single crystal data reported in the literature.[36] The ICP-OES results quantified the Mn content in ZIF-8 to be 0.017 wt% and the Mn/Zn ratio to be 0.00064 ($Zn_{0.999}Mn_{0.00064}(MeIm)_2$), followed by N_2 sorption measurements (SI, Fig. S2). Moreover, the TGA profile for Mn-ZIF-8 (SI, Fig. S1b) confirms that the thermal stability of the ZIF-8 framework is up to 400 °C without any significant mass loss. The SEM image (SI, Fig. S3) reveals an average particle size of 100 nm, exhibiting an unaltered morphology after Mn doping.

The X-band and Q-band CW EPR spectra of Mn-ZIF-8 recorded at room temperature and 20 K are shown in Fig. 2 and 3, respectively. The complete set of temperature-dependent X-band EPR spectra is displayed in SI, Fig. S4. The observed spectra exhibit a typical powder pattern of a single species A of Mn^{2+} ions in their $3d^5$ electronic high spin configuration with $S = 5/2$. The central allowed hyperfine (hf) sextets belonging to the $M_S = \frac{1}{2} \leftrightarrow -\frac{1}{2}$ (M_S – magnetic spin quantum number) along with the five forbidden hf doublets can be observed due to the hf interaction of the electron spin with the nuclear spin $I = 5/2$ of the ^{55}Mn nucleus. The total electron spin of Mn^{2+} being $S = 5/2$ leads to a ZFS, which, in addition to the central hyperfine sextet, gives rise to outer fine-structure (fs) transitions ($M_S = \pm1/2 \leftrightarrow \pm3/2$, $= \pm3/2 \leftrightarrow \pm5/2$) observed in the EPR spectra. Those outer fs transitions are not that well resolved for the activated Mn-ZIF-8 material, which is indicative of a small ZFS, as can be inferred from our spectral simulations (SI, Fig. S4).

All EPR spectra were simulated for quantitative analysis using the spin-Hamiltonian in eqn (1). Spectral simulation of CW EPR spectra of Mn-ZIF-8 recorded at room temperature and at 20 K at both X-band and Q-band are also shown in Fig. 2 and 3, respectively. Due to the limited microwave frequencies of our measurements, the anisotropy of the Zeeman interaction is not resolved; therefore, using isotropic $\boldsymbol{g}$ and $\boldsymbol{A}$ tensors proved to be sufficient for accurately reproducing the experimental spectra.[35] The spin Hamiltonian parameters used for simulation of the room temperature spectra at both microwave

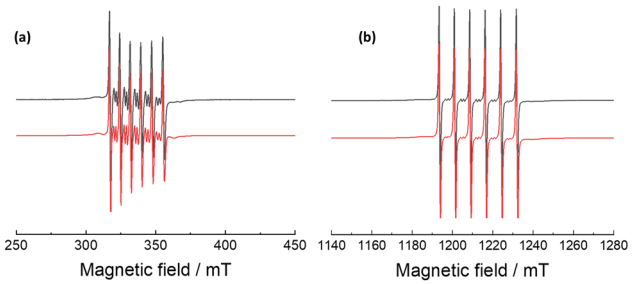

Fig. 2 Experimental (black) and simulated (red) CW EPR spectra of Mn-ZIF-8 at room temperature at (a) X-band and (b) Q-band.

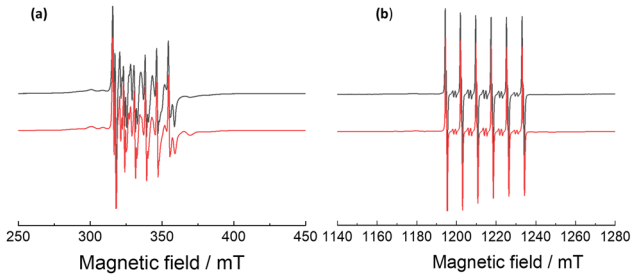

Fig. 3 Experimental (black) and simulated (red) CW EPR spectra of Mn-ZIF-8 at 20 K at (a) X-band and (b) Q-band.

frequencies are $g = 1.9988(2)$, $A = -215(1)$ MHz, $D = 200(10)$ MHz, $E = 0(5)$. Since the outer fs transitions are not resolved and only two shoulders at the low and high field side of the central hf sextet were observed, a Gaussian distribution of the parameter D with a full width half maximum (FWHM) of $\Delta D = 150(2)$ MHz was also used. Moreover, including the higher-order ZFS parameters B_4^0, B_4^2, B_4^3 and B_4^4 did not lead to a significant improvement of the simulated spectra of the activated Mn-ZIF-8 and were consequently set to zero for these simulations. For the spectral simulation of CW EPR spectra recorded at 20 K at both X-band and Q-band, comparable parameters $g = 1.9988(2)$ and $A = -217(1)$ MHz were obtained, whereas the ZFS parameters $D = 385(10)$ MHz, $E = 15(5)$ MHz and $\Delta D = 145(2)$ MHz slightly increased at the lower temperature. The temperature dependence of the CW EPR spectra of the Mn^{2+} species A is shown in Fig. S4 along with simulation parameters (see SI, Table S1). It was observed that the zero-field splitting parameter D slightly decreases continuously with increasing temperature (SI, Fig. S5).

Furthermore, *in situ* CW EPR gas adsorption experiments were carried out at $T = 66$ K to search for a potential effect of the gate opening phenomenon and the related AP ↔ HP structural transformation during N_2 adsorption and desorption processes on the Mn^{2+} EPR spectra. A selection of the recorded *in situ* CW EPR spectra during N_2 sorption process is illustrated in Fig. 4. The complete set of *in situ* spectra is presented in detail (SI, Fig. S6a). Again, the Mn^{2+} spin Hamiltonian parameters have been derived from spectra simulations for each pressure step (SI, Fig. S7). During N_2 adsorption, it is observed that at the lowest pressures (p/p^0 from 4.52×10^{-6} to 9.48×10^{-3}), comparable spectra as those for the activated Mn-ZIF-8 material were obtained (Fig. 5a) with Mn^{2+} EPR parameters similar to those of species A at $T = 66$ K as shown in Table 1. This indicates that no observable changes occur at the Mn^{2+} metal sites within this pressure range during N_2 adsorption. Upon further increase in pressure, at $p/p^0 = 1.82 \times 10^{-2}$, a second species with molar fraction of 0.1 (designated as B and characterized by the EPR parameters listed likewise in the Table 1) begins to appear alongside species A as illustrated in Fig. 5b. This new Mn^{2+} species B is characterised by a substantial larger ZFS parameter $D = 1050(10)$ MHz as the outer $M_S = \pm\frac{1}{2} \leftrightarrow \pm\frac{3}{2}, \pm\frac{3}{2} \leftrightarrow \pm\frac{5}{2}$ fs transitions are clearly resolved now. In contrast to species A,

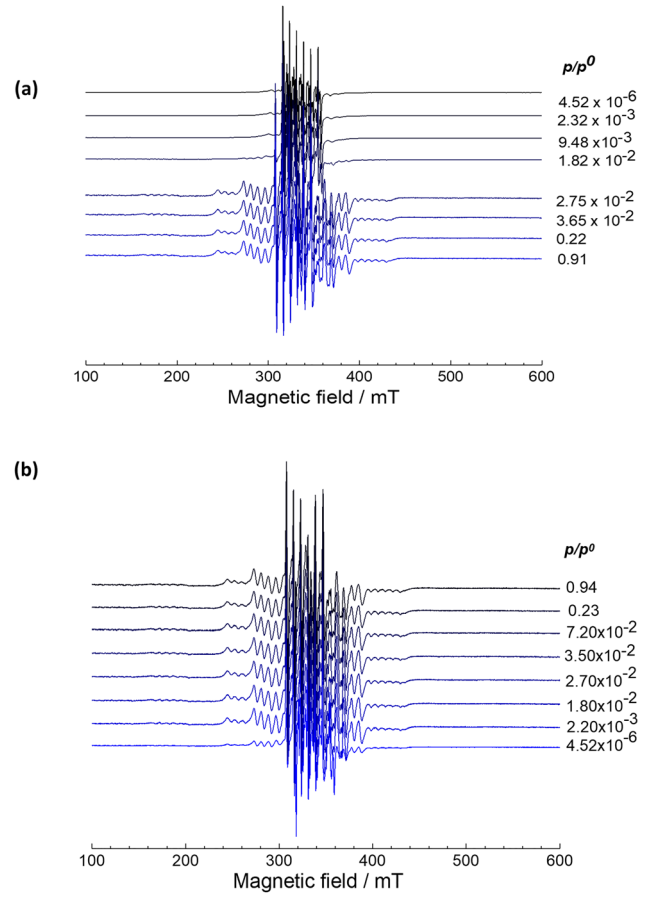

Fig. 4 *In situ* X-band CW EPR spectra of Mn-ZIF-8 during (a) N_2 adsorption and (b) N_2 desorption recorded at 66 K.

satisfactory simulations of species B were only achieved by including a high-order parameter B_4^0 = 0.20(6) MHz, while all remaining fourth-order parameters were still found to be zero within the accuracy of our simulation approach. In the pressure range from $p/p^0 = 2.75 \times 10^{-2}$ up to $p/p^0 = 0.91$, species A is completely absent, leaving only species B (Fig. 5c). The pronounced spectral changes at higher pressures (at $p/p^0 \leq 1.82 \times 10^2$) indicate transformation from species A to a new species B, which exhibits a larger ZFS parameter D, along with contributions from the fourth-order ZFS parameter B_4^0. *Ex situ* Q-band experiments on the sealed sample loaded with N_2 gas, provided likewise the spectrum of the species B (SI, Fig. S12) with identical spin Hamiltonian parameters. The evolution of species A and B during N_2 adsorption as deduced from their weights in the spectral simulations is illustrated in Fig. 7a.

Fig. 4b shows selected *in situ* EPR spectra of the Mn^{2+} spin probe in Mn-ZIF-8 during the desorption of N_2. The complete set of *in situ* spectra are presented in SI, Fig. S6b together with the corresponding spectral simulations in SI, Fig. S8. In the whole pressure range, species B dominates and 20% of species B persists even at the lowest pressure $p/p^0 = 4.52 \times 10^{-6}$ with 80% of species A being present. This means that a significant amount of N_2 gas remains confined within the pores despite the reduction in external gas pressure. The evolution of species

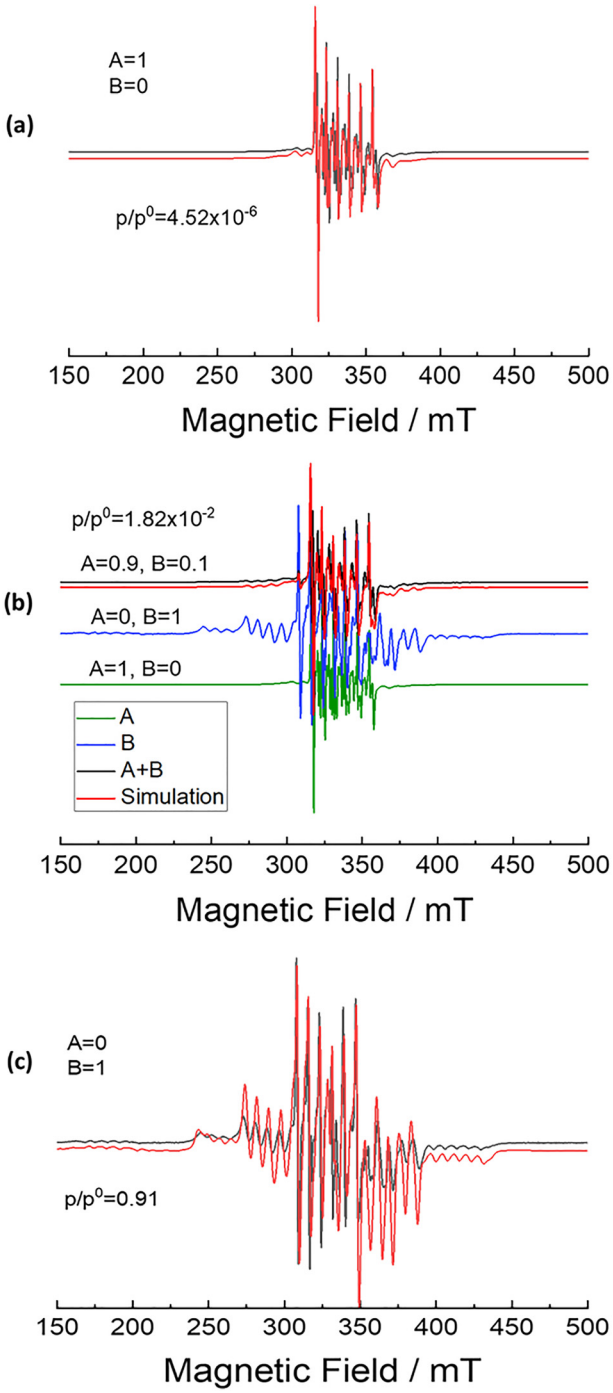

Fig. 5 Experimental (black) and simulated (red) CW EPR spectra of Mn-ZIF-8 measured during N_2 adsorption at (a) $p/p^0 = 4.52 \times 10^{-6}$, (b) $p/p^0 = 1.82 \times 10^{-2}$ and (c) $p/p^0 = 0.91$ and temperature 66 K.

A and B during N_2 desorption as obtained from the weights of their sub-spectra in the spectral simulations is presented in Fig. 7b. EPR spectra were also recorded at the lowest pressure while varying the waiting time to record the spectra to see if the remaining 20% of species B disappear over time (SI, Fig. S9). Notably, species B was still present even after a 45 minute waiting period although with less intensity. Complete

Table 1 Spin Hamiltonian parameters obtained by spectral simulations of Mn-ZIF-8 for species A and B at T = 66 K. The ZFS strain parameter for species A is ΔD = 140(10) MHz; and for species B are ΔD = 40(5) MHz and ΔE = 15(5) MHz

Species	g	A/MHz	$D = 3B_2^0$/MHz	$E = B_2^2$/MHz	B_4^0/MHz
A	2.0005(2)	−217(1)	350(10)	10(2)	0
B	2.00001(2)	−217(1)	1050(10)	15(0.75)	0.20(6)

desorption of N_2 gas was only achieved upon heating the sample to 77 K (SI, Fig. S9 and S10). Moreover, *in situ* CW EPR measurements were also recorded for Mn-ZIF-8 at 20 K under fixed N_2 gas loading of 100 mbar (Fig. 6a). At this temperature, the EPR spectra do not exhibit any spectral changes indicative of gas adsorption and the Mn^{2+} ions are present in the form of species A. The simulated parameters for species A in Fig. 6a are g = 1.9988(2) and A = −217(1) MHz, with the ZFS parameters as D = 385(10) MHz, E = 15(5) MHz and ΔD = 145(2).

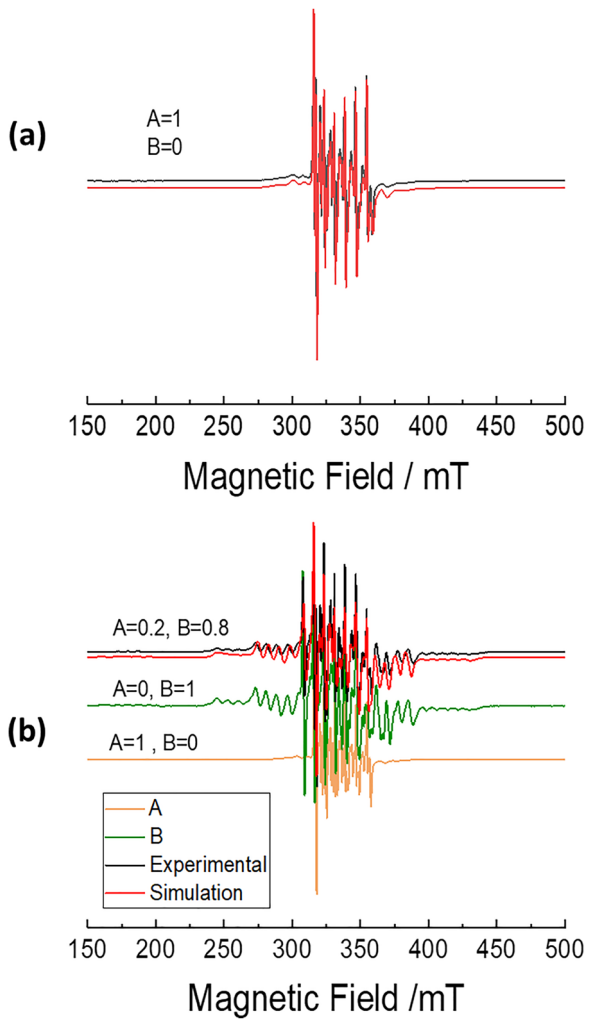

Fig. 6 Simulated (red) and experimental (black) *in situ* X-band EPR spectra of N_2 adsorbed Mn-ZIF-8 at (a) T = 20 K and (b) T = 60 K measured at 100 mbar.

Upon increasing the temperature to 60 K (Fig. 6b) with the pressure still being 100 mbar, significant spectral changes are observed, indicating the emergence of species B by 80%, while only 20% of species A is left. The simulated parameters for both species A and species B in Fig. 6b are shown in Table 1.

The detailed temperature dependence of Mn-ZIF-8 in the presence of N_2 gas was recorded in additional *ex situ* CW EPR measurements on a sealed sample at the X-band (SI, Fig. S11). Species A with only slightly increased parameters D = 350(20) MHz and ΔD = 350(10) MHz compared to the activated material at T = 11 K, dominates for T < 60 K with a weight of 70%, while at intermediate temperatures 60 K < T < 120 K, only species B with D = 1050(10) MHz can be observed. However, species B vanishes fully at temperatures above 100 K and species A reappears again. We have to note that unlike *in situ* experiments (Fig. 7a), a residual amount of species B can also be detected in the low temperature range T < 60 K with a weight of approximately 30% (SI, Fig. S11).

Cu-ZIF-8

As discussed in our previous work,[27] Cu^{2+} ions can be incorporated at Zn^{2+} sites in the ZIF-8 framework, which results in the formation of a distorted tetrahedral coordination geometry of the Cu^{2+} ions in ZIF-8. Such a distorted tetrahedral Cu^{2+} site may adopt a symmetry of either D_{4h} or D_{2d} as a result of the static Jahn–Teller effect and the constraint imposed by the methyl imidazolate linkers of the ZIF-8 framework.[27]

The ICP-OES analysis provided a copper content of 0.41 wt% and consequently a Cu/Zn ratio of 0.016 ($Zn_{0.984}Cu_{0.016}(MeIm)_2$) for Cu-ZIF-8 sample studied in this work. Fig. 8a illustrates the temperature dependence of the Cu^{2+} CW EPR spectra for the activated Cu-ZIF-8 MOF. The distorted tetrahedral Cu^{2+} coordination environment is reflected in the spectra at low temperatures T < 120 K, which shows a predominantly anisotropic CW EPR signal due to the coupling of an electron spin S = 1/2 to the $^{63,65}Cu$ (I = 3/2) nuclear spin. EPR spectral simulation suggests that the majority of the signal at 20 K (Fig. 8b) can be described by a cupric ion species with principal values of rhombic g-tensor of g_{zz} = 2.367(3), g_{yy} = 2.093(3) and g_{xx} = 2.088(2) and copper hf coupling parameters A_{zz} = 250(2) MHz, A_{yy} = 70(10) MHz and A_{xx} = 30(10) MHz.[27] We designate this Cu^{2+} moiety as

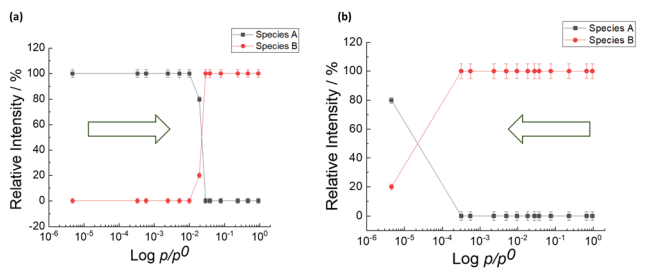

Fig. 7 Evolution of Mn^{2+} species A and B upon (a) N_2 adsorption (b) and N_2 desorption over Mn-ZIF-8 at 66 K. The relative intensity is obtained from the weighting factor of both the species used in the spectral simulations shown in SI, S7 and S8. It should be noted that the lines connecting the data points are just a guide to the eye.

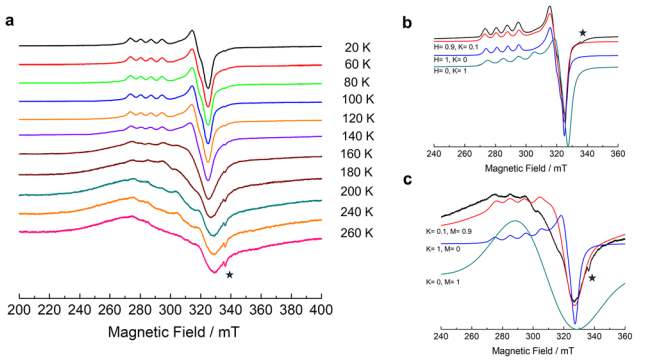

Fig. 8 (a) X-band CW EPR data of Cu-ZIF-8 recorded at several temperatures. (b) Spectral simulation for the CW EPR spectra at 20 K and (c) at 180 K. The experimental spectra are indicated in black, while the simulated spectra are depicted in red. In addition, the spectra of relevant species are provided to decompose the simulated spectra. The signal marked by a star symbol is caused by an additional minor radical species.

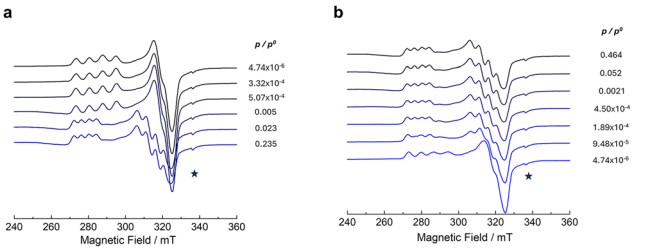

Fig. 9 (a) *In situ* X-band CW EPR data of Cu-ZIF-8 recorded during N_2 adsorption and (b) N_2 desorption recorded at 66 K (p^0 = 221 mbar). The signal marked by a star symbol is caused by an additional minor radical species.

Table 2 Spin Hamiltonian parameters obtained by spectral simulations for the Cu-ZIF-8 framework

Species	g_{xx}	g_{yy}	g_{zz}	A_{xx}/MHz	A_{yy}/MHz	A_{zz}/MHz
H	2.088(2)	2.099(2)	2.365(2)	50(10)	70(10)	240(10)
K	2.077(4)	2.077(4)	2.320(2)	70(10)	70(10)	310(10)
L	2.130(2)	2.130(2)	2.420(2)	130(10)	130(10)	140(10)
M	g_{iso} = 2.180(4)			A_{iso} = 140(20)		

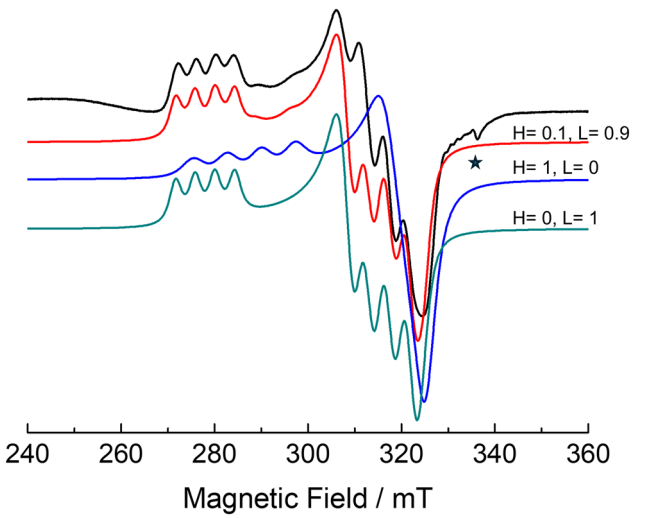

Fig. 10 The X-band CW EPR data of Cu-ZIF-8 recorded during N_2 adsorption at p/p^0 = 0.023 and a temperature of 66 K (in black). The red line indicates the simulated spectra using spin Hamiltonian parameters of species L as a representation of the HP phase. The signal marked by a star symbol is caused by an additional minor radical species.

species H in the following. There is a minor contribution (10%) in the spectrum of Cu-ZIF-8 from another Cu^{2+} species K with g_{zz} = 2.320(3) and A_{zz} = 310(10), which seems to be present in the whole studied temperature range 20 K $\leq T \leq$ 260 K (SI, Fig. S13a). As the temperature increases the intensity of the major cupric ion species H decreases drastically and a broad signal of a new species M develops superimposed by the spectral features of the minor species K. Although difficult, as the correct line shape of this broad signal of the Cu^{2+} species M is not known and can only be approximated by an isotropic Gaussian line shape, we attempted to simulate the whole temperature dependence of the Cu^{2+} EPR spectra of Cu-ZIF-8 by taking into account the three signals of the species H, K, and M (Fig. 8c and SI, Fig. S13).

The simulation reveals that as the temperature is increased to 140 K, the weight of species H reduces significantly to 50% whereas the additional species M needs to be included in the simulation with 20% of weight (Fig. S13c). Species M can be approximated in the simulations by an isotropic *g*-factor of 2.180(4), an isotropic hf coupling A_{iso} = 140(20) MHz and a Gaussian linewidth of about 40 mT. Species M predominates in the CW EPR spectra of Cu-ZIF-8 at $T \geq$ 160 K, with the weight of more than 60% and it is accompanied by the minor species K, which is present already at lower temperatures. A plot of the derived copper *g* values and hf interaction parameters of species H and M together with their relative intensities as a function of temperature is provided in SI, Fig. S13b and c.

In situ CW EPR experiments of Cu-ZIF-8 were conducted to explore the influence of the gate-opening process during the N_2 adsorption and desorption on the cupric ions incorporated at the Zn^{2+} framework sites (Fig. 9a and b). It can be seen that after the activation process up to N_2 pressures of p/p^0 = 0.005, the EPR spectra resemble that of the Cu^{2+} species H. Then, at p/p^0 = 0.023, the CW-EPR spectra suddenly evolved to a new cupric ion species L with much higher g_{zz} (2.420) and significantly smaller A_{zz} (140 MHz) parameters (Table 2 and Fig. 9a). It is also obvious from spectral simulations (Fig. 10 and SI, Fig. S18) that the A_{xx} or A_{yy} parameters have increased significantly as opposed to the EPR parameters for species H. The evolution of species H and species L in terms of their weights in the spectral simulations as a function of log p/p^0 during N_2 adsorption is presented in Fig. 11a. Moreover, Fig. S14 provides the data on the effect of the waiting time (in the range of 1 min to 13 min) before the EPR spectral acquisition on such spectral changes due to N_2 adsorption at p/p^0 = 0.023 and 66 K. The weight of species H is slowly lowered, and the contribution of species L is increased until it completely dominates the spectral pattern after 13 min exposure to N_2 gas at p/p^0 = 0.023 and 66 K.

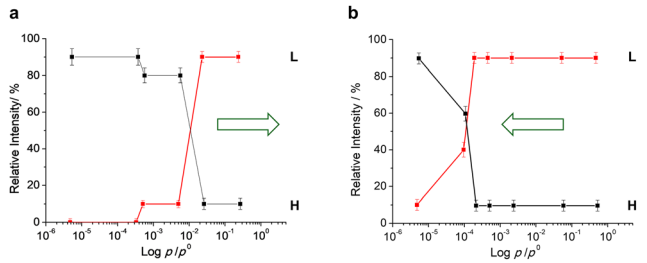

Fig. 11 Evolution of Cu^{2+} species H and L during (a) N_2 adsorption and (b) N_2 desorption processes over Cu-ZIF-8 at 66 K. The relative intensity is deduced from the weighing factor of each species in the spectral simulations in Fig. S14 and S15. Again, the lines joining the data points are just a guide to the eye.

On the other hand, the desorption process of N_2 gas from the ZIF-8 frameworks depicted in Fig. 9b and 11b also triggers the evolution of CW EPR spectra from a predominantly species L to the initial state (predominantly species H) only at $p/p^0 \approx 4.74 \times 10^{-6}$ although with relatively more broadening of the copper hf lines in the g_{zz} spectral range (270–300 mT) of the Cu^{2+} powder patterns (simulated by applying anticorrelated g_{zz} strain of 0.028 and A_{zz} strain parameters of 30 MHz for species H) in comparison to the initial state of species H before the N_2 adsorption. Fig. 11b shows the evolution of species H and species L proportions obtained by spectral simulations as a function of pressure for the N_2 desorption process.

Again, the influence of the waiting time (in the range of 2 min to 45 min) before recording the EPR spectrum on the cupric ion signal during desorption at $p/p^0 = 4.74 \times 10^{-6}$ and 66 K of N_2 at $p/p^0 = 4.74 \times 10^{-6}$ and 66 K is investigated (Fig. S15). It is obvious that the time taken to induce the spectral transformation of species L back to species H is comparatively shorter than the spectral transformation from species H to species L for the adsorption case.

The effect of temperature on the desorption of N_2 is presented in SI, Fig. S17. These experiments reveal that the Cu^{2+} spectra of the species H can only be recovered to the initial state without any line broadening due to anticorrelated g_{zz} and A_{zz} by increasing the temperature from 66 K to 77 K while pumping the N_2 out of the pores.

Discussion

The EPR investigations of the activated Mn-ZIF-8 MOF revealed a Mn^{2+} species A with ZFS parameters of D varying between 385 MHz and 200 MHz and E between 0 and 15 MHz in the temperature range 11 K $\leq T \leq$ 280 K and a constant isotropic hf coupling A = 217 MHz. The latter may provide some insight into the type of coordinating ligands Y and their number n as there exists a phenomenological relation between the isotropic hf coupling of Mn^{2+} ions and Pauling's covalency parameter ρ of the substitutional manganese cluster MnY_n in the solid.[34] The quantity ρ is obtained from the ratio between the electronegativity differences, $\chi_M - \chi_L$, between the manganese ion and the coordinating donor atoms Y and their number n[37]

$$\rho = \frac{1 - 0.16(\chi_Y - \chi_M) - 0.035(\chi_Y - \chi_M)^2}{n}. \quad (2)$$

If the nitrogen atoms from the imidazolate linkers are the only possible coordinating atoms to the Mn^{2+} ions and taking the Pauling electronegativity values χ_{Mn} = 1.5 eV and χ_N = 3.0 eV, we can calculate the covalency parameter ρ for the reasonable coordination numbers n = 4, 5, and 6 (SI, Table S4). Based on the value ρ = 0.17 for n = 4 and the phenomenological relation between ρ and A as presented in the paper by Šimánek *et al.*[37] we find that the experimentally obtained isotropic hf coupling 217 MHz of the Mn^{2+} ions in Mn-ZIF-8 is close to the expected one of a MnN_4 unit of 206 MHz (SI, Table S4) confirming the substitution of the tetrahedrally coordinated Zn^{2+} by the paramagnetic Mn^{2+} probe ions. Indeed, comparable hyperfine parameters were found for divalent manganese dopants in AlN (193 MHz)[38] and GaN[39] with likewise tetrahedral nitrogen coordination environment.

The observed ZFS parameters D and E of the Mn^{2+} ions in activated Mn-ZIF-8 indicate subtle axial and even smaller orthorhombic distortions of the MnN_4 tetrahedral environment in agreement with the somewhat larger deviation of the bond angles of the MnN_4 units from the perfect tetrahedral angle for the pure manganese substituted ZIF-8(Mn) system[28] in comparison with those of the ZnN_4 units in parent ZIF-8(Zn) (SI, Table S3). Furthermore, the observed D values fall within the range reported by Duboc *et al.*[40] for other systems with nitrogen coordinating to Mn^{2+} ions and are in agreement with the assignment of species A to a distorted tetrahedral MnN_4 unit. We have to note that in the case of the aluminophosphate AlPO-5 a tetrahedral oxygen coordination of the Mn^{2+} ions leads to a similar D parameter.[41]

The increase of the Mn^{2+} ZFS parameter D found with decreasing temperature is a common phenomenon for solid systems[34] and has partly been assigned to lattice-vibration effects coupled to the Mn^{2+} centre[42] and to the thermal contraction of the lattice.[43]

The adsorption of N_2 gas over Mn-ZIF-8 at 66 K has a significant impact on its Mn^{2+} EPR spectrum and leads to complete transformation of species A to species B with significantly larger axial ZFS parameter D (Table 1). This transformation sets in at $p/p^0 = 1.82 \times 10^{-2}$ with a superposition of 10% species B and 90% of species A initially. Species B becomes the sole contributor to the Mn^{2+} spectrum at a pressure of $p/p^0 = 2.75 \times 10^{-2}$ and remains this up to the highest studied pressure p/p^0 = 0.91. It is important to note that the previously reported gate-opening and the corresponding AP to HP structural transformation of ZIF-8 appear at a comparable pressure/$p^0 \approx 0.02$) and temperature (T = 60–80 K) as initially found from volumetric N_2 adsorption data and verified by neutron scattering experiments.[6,7] Therefore, it seems justified to assign species A to Mn^{2+} probe ions located in the AP phase and species B to those present in the HP phase. The Mn^{2+} spin probes monitor the swinging motion of imidazolate ligands and the related

gate opening due to structural changes at the tetrahedral MnN_4 units leading to a larger axial distortion, as a result of the larger ZFS parameter D. Consequently, the relative intensities of the Mn^{2+} EPR spectra of species A and B can be considered as measures for the molar fraction of the AP to HP phases, respectively, at a given pressure and temperature (Fig. 8). Interestingly, this AP $\leftrightarrow$ HP transition as monitored by the Mn^{2+} spin probes, which takes place in a narrow pressure range $1.82 \times 10^{-2} \leq p/p^0 \leq 2.75 \times 10^{-2}$ at $T = 66$ K, is prevented at lower temperatures ($T \leq 40$ K) even if the sample is subjected to substantial high pressures of the N_2 gas $p/p^0 \geq 2.75 \times 10^{-2}$ (Fig. 6 and SI, Fig. S11). The gate opening sets in under such conditions only if the temperature is raised above 40 K.

It is very important to note that while N_2 desorption at $T = 66$ K, 20% of species B and consequently the HP phase were present even at the lowest pressure (Fig. 7a). Hence, our observation of such pronounced hysteresis effects in the N_2 sorption behaviour reflects that the system does not completely relax the structure back to the initial AP phase because of energetic barriers,[44] while some fraction of the sample still lingers in the HP phase at the lowest pressure $p/p^0 = 4.5 \times 10^{-6}$. Upon thermal activation, such energetic barriers between the AP and HP phases are overcome.[44] Consequently, N_2 desorption is fully reversible, as evidenced by the restoration of the original EPR spectrum upon heating the sample to 77 K at the lowest relative pressure ($p/p^0 = 4.5 \times 10^{-6}$) (SI, Fig. S9).

In order to verify the *in situ* EPR results obtained for Mn-ZIF-8 upon N_2 sorption, we employed a second spin probe, namely Cu^{2+} ions. In contrast to the Mn^{2+} spin probes in Mn-ZIF-8, the Cu^{2+} species in MOF Cu-ZIF-8 exhibit more distortions in terms of bond angles (see SI, Table S3) in their tetrahedral CuN_4 environment within the ZIF-8 framework.[45,46] In principle, such distortions could be attributed to a static Jahn–Teller effect at the distorted tetrahedral Cu^{2+} ($3d^9$) site, as opposed to Mn^{2+} ($3d^5$ ions), due to differences in their electronic configuration.[47] In terms of a local structure, it is also worth noting that the Mn–N and Cu–N bonding properties (bond angle N–M–N and bond distance M–N, M = Mn, Cu) deviate from the pure Zn–N bonds in the tetrahedral ZnN_4 unit of the parent ZIF-8(Zn) structure, which subsequently determines the overall stability of the M^{2+} doped ZIF-8 structure. ZIF-8(Mn) with 100% content of Mn exists, for example, but is unstable under ambient air due to Mn^{2+} affinity toward H_2O molecules,[28] whereas Cu-ZIF-8 is only stable with a maximum 20% Cu^{2+} content as a result of relatively longer M–N bond distance and smaller formation energy of Cu-ZIF-8, respectively.[27]

The temperature-dependence of the EPR parameters for Cu^{2+} speciation in the absence of gas is marked by the changes of g-tensor and Cu hf coupling parameters from the anisotropic species H to the isotropic species M at $T > 140$ K (Fig. 8). Fig. S13c (SI) indicates that at a lower temperature (40 K), two species coexist with species H as a favoured species according to the simulation (90% of species H and 10% of species K). As the temperature increases to $T > 150$ K, species M gradually predominates with a trace amount of species K. The g_{iso} and A_{iso} of species M correspond to the average values of the anisotropic g-tensor and Cu hf interaction parameters from species H, which provides us with a hint that species M basically originated from species H.

Hoffmann and Ulanov reported the g-factor averaging with increasing temperature for the Cu^{2+} centre in a SrF_2 crystal,[48] attributed to a dynamic Jahn–Teller effect.[49,50] Likewise, Silver and Getz[51] described a similar effect for a Cu^{2+} doped Zn^{2+} Tutton's salt where the cupric ions may exhibit three octahedrally distorted $Cu^{2+}(H_2O)_6$ configurations with very close potential energy surfaces. In analogy, Cu^{2+} ions in a tetrahedral coordination environment can likewise undergo a dynamic Jahn–Teller effect.[52] Previous EPR studies at 10 K revealed a distortion of the CuN_4 units towards a flattened tetrahedral metal ion coordination.[27] Therefore, it is natural to assume that at lower temperatures ($T < 140$ K), species H is the most stable configuration of such distorted flattened tetrahedral Cu^{2+} species. However, at higher temperatures ($T > 140$ K), the stability of species H in the form of such a tetrahedrally distorted Cu^{2+} is significantly reduced, resulting in faster rates of exchange between the most likely three Cu^{2+} configurations of the flattened tetrahedral CuN_4 unit[27] with similar potential energy surface leading to the formation of an isotropic species M.

In the majority of cases reported for the dynamic Jahn–Teller effect, *e.g.* in ionic solids, the anisotropic low temperature and averaged high temperature Cu^{2+} species do not coexist in the same temperature range. However, a co-existence of both Cu^{2+} species is not uncommon, and several cases have been reported.[53–55] For instance, Kahn and co-workers[53] observed the co-existence of anisotropic and isotropic copper spectra in the case of an octahedrally distorted Cu^{2+} species doped into a $[Fe(NH_2trz)_3](NO_3)_2$ crystal. These species coexisted over a broad range of temperatures, and they attributed this to a distribution of the energy difference between the lowest and the higher valleys of the Jahn–Teller potential energy resulting from crystal disorder. In the current study, the co-existence of the Cu^{2+} species H and M indicate likewise a distribution in potential energy differences for the substitutional copper sites in ZIF-8. However, this is probably rather driven by the diversity of the Cu^{2+} environment in the ZIF-8 frameworks instead of crystal disorder.

The presence of N_2 gas within the pores of Cu-ZIF-8 likely promotes an alternative stabilisation pathway for Cu^{2+}, favouring a less-distorted tetrahedral environment (species L) (Fig. 9a). This is evidenced by the significant increase in the g_{zz} value and decrease in the A_{zz} parameter. Please note that Cu^{2+} species L has unusual hyperfine coupling trends due to its substantial "perpendicular" hyperfine component (A_{xx} and A_{yy}). However, for the distorted tetrahedral Cu^{2+}, such a peculiar trend is not new, as in 1967, Sharnoff[56] studied $CuCl_4^-$ (D_{2d}) in a single crystal of Cs_2CuCl_4 and Cs_2ZnCl_4 with the A_{xx} (150 MHz) exceeding A_{zz} (75 MHz) parameters. Sharnoff interpreted the substantial reduction of A_{zz} found for $CuCl_4^-$ (D_{2d}) (in comparison to the elongated octahedral or square planar Cu^{2+} coordination geometries) by a direct $4p_z$ (Cu) admixture into the ground-state wavefunction of Cu^{2+} ($3d_{xy}$). On the other hand, the covalency of Cu–Cl bonding and significant

spin–orbit coupling of Cl may also play a role in the hyperfine parameter reduction.[57] However, Hitchman[58] explained that the reduction of A_{zz} parameter originates from the energy decrease of the excited d states resulting in a larger contribution of the interaction between the copper nuclear spin and the orbital angular momentum to the hf interaction. Furthermore, Solomon and colleagues[59] reported experimental and theoretical studies on Cu-doped bis(1,2-dimethylimidazole)zinc(II) dichloride, and verified by self-consistent field Xα-scattered wave calculations the enhanced contribution of the orbital dipolar contribution to the Cu^{2+} hf parameters. In addition, they clarified a further contribution to the A_{zz} and $A_{xx,yy}$ parameters, which becomes significant for cupric ions in D_{2d} symmetry, an increase of spin polarisation from the valence 4s orbital. A direct 4s or $4p_z$ admixing into the $3d_{xy}$ ground state was found to be negligible.

The Jahn–Teller distortion of Cu^{2+} may be compensated by the gate-opening motion of the framework, which stabilises the HP phase of ZIF-8 and accommodates a more symmetric coordination around the Cu^{2+} centre. As the pressure range $5.74 \times 10^{-4} \leq p/p^0 \leq 2.3 \times 10^{-2}$ at $T = 66$ K to transform the *in situ* EPR spectra of Cu^{2+} species H to species L is within the pressure range for the AP → HP structural transformation obtained for the Mn^{2+} probes, we can again assign these spectral changes to the gate opening of ZIF-8. We are further allowed to consider the relative intensities of the cupric ion species H and L to be proportional or the molar fraction of the AP and HP phases (Fig. 11). The *in situ* EPR experiments on the Cu^{2+} spin probes in Cu-ZIF-8 revealed for the N_2 desorption branch comparable strong hysteresis effects as for Mn-ZIF-8 (Fig. 9b and 11b).

It is important to note that both Mn^{2+} and Cu^{2+} ions that have been incorporated at Zn^{2+} lattice sites into the ZIF-8 framework, sense, as observed by other experimental techniques,[6,7] the AP → HP pore transformation by their spin Hamiltonian parameters, which signifies their reliability as spin probes to monitor local structural changes as a response to the N_2-induced gate-opening or closing phenomenon in the doped ZIF-8 materials. In addition, the local structural changes on both Mn^{2+} and Cu^{2+} are sensitive for tracing the back-transformation from the HP to the AP phase during N_2 desorption from ZIF-8 under variable temperatures. Moreover, this *in situ* EPR study with variable waiting times in the spectral acquisition at selected gas pressures p/p^0 also indirectly suggests that the kinetic rates of gate-opening in ZIF-8 proceed comparatively faster than the pore-closing or pore contraction, commonly observed in some other MOFs with gate-opening behaviour.[25,60,61]

Conclusions and outlook

In this contribution, temperature-dependent CW-EPR measurements were carried out on both Mn-ZIF-8 and Cu-ZIF-8 to probe potential structural changes within the ZIF-8 framework. Both ions replace Zn^{2+} at their tetrahedral lattice sites. Our analysis reveals that the local structure of the Mn^{2+} ions is relatively stable in response to the temperature modulation, whereas Cu^{2+} ions, already leading to substantial distortion of the metal ion tetrahedra, undergo a dynamic Jahn–Teller effect at elevated temperatures. Furthermore, the presence of N_2 gas within the pores induces the local structure transformation into a more distorted, but still, almost axially symmetric tetrahedral Mn^{2+} species while it stabilises a more symmetric, less distorted tetrahedral Cu^{2+} coordination, suggesting that framework flexibility and gas–metal ion interactions modulate the electronic and local structure environment of the metal dopant ions in the ZIF-8 framework according to the properties of the metal ions themselves. Other than the ZnN_4 units both CuN_4 and MnN_4 are subjected to structural changes at the AP ↔ HP structural transition. We conclude that the swinging effect of the imidazolate linker influences the structure of these metal ions in tetrahedral environment. The gate-opening, AP ↔ HP structural transformation, observed *via in situ* CW EPR of both Mn^{2+} and Cu^{2+}, is reflected by the changes in the zero-field splitting parameters on Mn^{2+} as well as *g*-factor and copper hyperfine coupling parameter changes on Cu^{2+}, respectively. Furthermore, the pressure of gate-opening obtained *via in situ* EPR spectroscopy matches very well with the gate-opening pressure reported *via* N_2 adsorption isotherm data and neutron scattering data at comparable temperatures, underscoring the effectiveness of spin probes for detecting subtle framework dynamics during gas sorption processes in the ZIF-8 on the local scale.

Author contributions

Antareekshya Deka: conceptualization, investigation, data curation, writing – original draft, and writing – review and editing. Muhammad Fernadi Lukman: investigation, data curation, writing – review and editing. Sibo Chetry: synthesis, characterization, writing – review and editing. Christian Jänke: synthesis, writing – review and editing. Harald Krautscheid: review and supervision. Andreas Pöppl: conceptualization, methodology, writing – review and editing, supervision, project administration and funding acquisition.

Conflicts of interest

There are no conflicts to declare.

Data availability

All data supporting this article have been deposited in Zenodo at https://doi.org/10.5281/zenodo.17724954.

The data supporting this article have been included as part of the supplementary information (SI). Supplementary information is available. See DOI: https://doi.org/10.1039/d5cp04761g.

Acknowledgements

This work was funded by the German Research Foundation (DFG), Project number 514664767, TRR-386: ''HYP*MOL – Hyperpolarization in molecular systems'' and Project ID 443871192, GRK 2721: ''Hydrogen Isotopes 1,2,3H''. We thank Dr David Poppitz and Prof. Dr Roger Gläser from the Institute of Technical Chemistry, Leipzig University, for the SEM images. We also thank Dr Paolo Cleto Bruzzese from the Department of Chemistry, University of Torino, for the fruitful discussions.

References

1 B. Li, H. M. Wen, Y. Cui, W. Zhou, G. Qian and B. Chen, *Adv. Mater.*, 2016, **28**, 8819–8860.
2 M. Ding, X. Cai and H. L. Jiang, *Chem. Sci.*, 2019, **10**, 10209–10230.
3 N. C. Burtch, H. Jasuja and K. S. Walton, *Chem. Rev.*, 2014, **114**, 10575–10612.
4 P. Horcajada, R. Gref, T. Baati, P. K. Allan, G. Maurin, P. Couvreur, G. Férey, R. E. Morris and C. Serre, *Chem. Rev.*, 2012, **112**, 1232–1268.
5 M. Alhamami, H. Doan and C. H. Cheng, *Materials*, 2014, **7**, 3198–3250.
6 D. Fairen-Jimenez, S. A. Moggach, M. T. Wharmby, P. A. Wright, S. Parsons and T. Düren, *J. Am. Chem. Soc.*, 2011, **133**, 8900–8902.
7 M. E. Casco, Y. Q. Cheng, L. L. Daemen, D. Fairen-Jimenez, E. V. Ramos-Fernandez, A. Ramirez-Cuesta and J. Silvestre-Albero, *Chem. Commun.*, 2016, **52**, 3639–3642.
8 K. S. Park, Z. Ni, A. P. Côté, J. Y. Choi, R. Huang, F. J. Uribe-Romo, H. K. Chae, M. O'Keeffe and O. M. Yaghi, *Proc. Natl. Acad. Sci. U. S. A.*, 2006, **103**, 10186–10191.
9 J. Pérez-Pellitero, H. Amrouche, F. R. Siperstein, G. Pirngruber, C. Nieto-Draghi, G. Chaplais, A. Simon-Masseron, D. Bazer-Bachi, D. Peralta and N. Bats, *Chem. – Eur. J.*, 2010, **16**, 1560–1571.
10 H. Tanaka, S. Ohsaki, S. Hiraide, D. Yamamoto, S. Watanabe and M. T. Miyahara, *J. Phys. Chem. C*, 2014, **118**, 8445–8454.
11 C. O. Ania, E. García-Pérez, M. Haro, J. J. Gutiérrez-Sevillano, T. Valdés-Solís, J. B. Parra and S. Calero, *J. Phys. Chem. Lett.*, 2012, **3**, 1159–1164.
12 D. Fairen-Jimenez, R. Galvelis, A. Torrisi, A. D. Gellan, M. T. Wharmby, P. A. Wright, C. Mellot-Draznieks and T. Düren, *Dalton Trans.*, 2012, **41**, 10752–10762.
13 F. Formalik, B. Mazur, M. Fischer, L. Firlej and B. Kuchta, *J. Phys. Chem. C*, 2021, **125**, 7999–8005.
14 G. Kumari, K. Jayaramulu, T. K. Maji and C. Narayana, *J. Phys. Chem. A*, 2013, **117**, 11006–11012.
15 M. E. Casco, J. Fernández-Catalá, Y. Q. Cheng, L. L. Daemen, A. J. Ramirez-Cuesta, C. Cuadrado-Collados, J. Silvestre-Albero and E. V. Ramos-Fernández, *ChemistrySelect*, 2017, **2**, 2750–2753.
16 C. L. Hobday, T. D. Bennett, D. Fairen-Jimenez, A. J. Graham, C. A. Morrison, D. R. Allan, T. Düren and S. A. Moggach, *J. Am. Chem. Soc.*, 2018, **140**, 382–387.
17 T. Tian, M. T. Wharmby, J. B. Parra, C. O. Ania and D. Fairen-Jimenez, *Dalton Trans.*, 2016, **45**, 6893–6900.
18 S. A. Moggach, T. D. Bennett and A. K. Cheetham, *Angew. Chem., Int. Ed.*, 2009, **48**, 7087–7089.
19 R. Boada, J. Chaboy, S. Hayama, L. L. Keenan, A. A. Freeman, M. Amboage and S. Díaz-Moreno, *J. Phys. Chem. C*, 2022, **126**, 5935–5943.
20 A. Sutrisno, V. V. Terskikh, Q. Shi, Z. Song, J. Dong, S. Y. Ding, W. Wang, B. R. Provost, T. D. Daff, T. K. Woo and Y. Huang, *Chem. – Eur. J.*, 2012, **18**, 12251–12259.
21 J. G. Vitillo and L. Gagliardi, *Chem. Mater.*, 2021, **33**, 4465–4473.
22 M. Mendt, P. Vervoorts, A. Schneemann, R. A. Fischer and A. Pöppl, *J. Phys. Chem. C*, 2019, **123**, 2940–2952.
23 M. Mendt, F. Gutt, N. Kavoosi, V. Bon, I. Senkovska, S. Kaskel and A. Pöppl, *J. Phys. Chem. C*, 2016, **120**, 14246–14259.
24 M. F. Lukman, S. Chetry, P. Sarkar, V. Bon, K. Thangavel, S. Kaskel, M. Hirscher, H. Krautscheid and A. Pöppl, *Chem. – Eur. J.*, 2025, **31**, e202500088.
25 M. F. Lukman, M. Mendt, V. Bon, S. Kaskel and A. Pöppl, *Chem. Commun.*, 2023, **59**, 9884–9887.
26 K. Thangavel, F. Walenszus, M. Mendt, V. Bon, S. Kaskel and A. Pöppl, *J. Phys. Chem. C*, 2023, **127**, 8217–8234.
27 M. F. Lukman, P. C. Bruzzese, W. Böhlmann, A. Schnegg and A. Pöppl, *J. Phys. Chem. C*, 2024, **128**, 9130–9141.
28 K. Kadota, E. Sivaniah, S. Bureekaew, S. Kitagawa and S. Horike, *Inorg. Chem.*, 2017, **56**, 8744–8747.
29 A. Schejn, A. Aboulaich, L. Balan, V. Falk, J. Lalevée, G. Medjahdi, L. Aranda, K. Mozet and R. Schneider, *Catal. Sci. Technol.*, 2015, **5**, 1829–1839.
30 S. Stoll and A. Schweiger, *J. Magn. Reson.*, 2006, **178**, 42–55.
31 M. Navickas, L. Giriūnas, V. Kalendra, T. Biktagirov, U. Gerstmann, W. G. Schmidt, M. Mączka, A. Pöppl, J. Banys and M. Šimėnas, *Phys. Chem. Chem. Phys.*, 2020, **22**, 8513–8521.
32 C. Rudowicz and C. Y. Chung, *J. Phys.: Condens. Matter*, 2004, **16**, 5825.
33 I. D. Ryabov, *Appl. Magn. Reson.*, 2009, **35**, 481–494.
34 V. K. Jain and G. Lehmann, *Phys. Status Solidi B*, 1990, **159**, 495–544.
35 M. Šimenas, A. Ciupa, M. Maczka, A. Pöppl and J. Banys, *J. Phys. Chem. C*, 2015, **119**, 24522–24528.
36 E. De Zitter, D. Perl, M. Savko, D. W. Paley, A. J. Thom, D. Jeangerard, A. S. Brewster, A. Tissot, C. Serre and W. Shepard, *CrystEngComm*, 2024, **26**, 5644–5654.
37 E. Šimánek and K. A. Müller, *J. Phys. Chem. Solids*, 1970, **31**, 1027–1040.
38 T. Graf, M. Gjukic, M. Hermann, M. S. Brandt, M. Stutzmann and O. Ambacher, *Phys. Rev. B:Condens. Matter Mater. Phys.*, 2003, **67**, 165215.
39 P. G. Baranov, E. N. Mokhov, A. O. Ostroumov, M. G. Ramm, V. V. Ratnikov, A. D. Roenkov, Y. A. Vodakov, A. A. Wolfson,

G. V. Saparin, S. Y. Karpov, D. V. Zimina, Y. N. Makarov and H. Juergensen, *Mater. Res. Soc. Internet J. Nitride Semicond. Res.*, 1998, **3**, 50.
40 C. Duboc, M. N. Collomb and F. Neese, *Appl. Magn. Reson.*, 2010, **37**, 229.
41 Z. Levi, A. M. Raitsimring and D. Goldfarb, *J. Phys. Chem.*, 1991, **95**, 7830–7838.
42 R. A. Serway, *Phys. Rev. B*, 1971, **3**, 608–615.
43 A. Manoogian, *J. Magn. Reson.*, 1979, **36**, 1–6.
44 I. Senkovska, V. Bon, L. Abylgazina, M. Mendt, J. Berger, G. Kieslich, P. Petkov, J. L. Fiorio, J.-O. Joswig, T. Heine, L. Schaper, C. Bachetzky, R. Schmid, R. A. Fischer, A. Pöppl, E. Brunner and S. Kaskel, *Angew. Chem., Int. Ed.*, 2023, **62**, e202218076.
45 C. P. Keijzers, T. Jansen, E. de Boer, G. van Kalkeren and J. S. Wood, *J. Magn. Reson.*, 1983, **52**, 211–220.
46 A. Le Nestour, M. Gaudon, G. Villeneuve, R. Andriessen and A. Demourgues, *Inorg. Chem.*, 2007, **46**, 2645–2658.
47 U. Öpik and M. H. Lecorney Pryce, *Proc. R. Soc. London, Ser. A*, 1957, **238**(1215), 425–447.
48 S. K. Hoffmann and V. A. Ulanov, *J. Phys.: Condens. Matter*, 2000, **12**, 1855.
49 F. S. Ham, *Phys. Rev.*, 1965, **138**, A1727.
50 M. A. Hitchman, C. J. Simmons and H. Stratemeier, *Appl. Magn. Reson.*, 2000, **19**, 121–131.
51 B. L. Silver and D. Getz, *J. Chem. Phys.*, 1974, **61**, 638–650.
52 C. A. Bates and P. E. Chandler, *J. Phys. C:Solid State Phys.*, 1973, **6**, 1975.
53 C. Cantin, H. Daubric, J. Kliava and O. Kahn, *Solid State Commun.*, 1998, **108**, 17–22.
54 A. M. Vorotynov, G. A. Petrakovskiĭ, K. A. Sablina, A. F. Bovina and A. D. Vasil'ev, *Phys. Solid State*, 2010, **52**, 2415–2418.
55 K. Mack, A. Wünsche von Leupoldt, C. Förster, M. Ezhevskaya, D. Hinderberger, K. W. Klinkhammer and K. Heinze, *Inorg. Chem.*, 2012, **51**, 7851–7858.
56 M. Sharnoff, *J. Chem. Phys.*, 1965, **42**, 3383–3395.
57 A. Bencini, D. Gatteschi and C. Zanchini, *J. Am. Chem. Soc.*, 1980, **102**, 5234–5237.
58 M. A. Hitchman, *Inorg. Chem.*, 1985, **24**, 4762–4765.
59 A. A. Gewirth, S. L. Cohen, H. J. Schugar and E. I. Solomon, *Inorg. Chem.*, 1987, **26**, 1133–1146.
60 M. Mendt, M. Maliuta, S. Ehrling, F. Schwotzer, I. Senkovska, S. Kaskel and A. Pöppl, *J. Phys. Chem. C*, 2022, **126**, 625–633.
61 H. Miura, V. Bon, I. Senkovska, S. Ehrling, N. Bönisch, G. Mäder, S. Grünzner, A. Khadiev, D. Novikov, K. Maity, A. Richter and S. Kaskel, *Adv. Mater.*, 2023, **35**, 2207741.

